Activation of magnetic moments by annealing in chemical vapor deposited graphene

Hyungki Shin,[*] Ebrahim Sajadi, Ali Khademi,[†] Silvia Lüscher, and Joshua A. Folk[‡]
Stewart Blusson Quantum Matter Institute, University of British Columbia, Vancouver, British Columbia V6T1Z4, Canada and Department of Physics and Astronomy, University of British Columbia, Vancouver, British Columbia V6T1Z1, Canada

(Received 9 July 2021; revised 8 October 2021; accepted 2 May 2022; published 12 May 2022)

The effects of annealing on chemical vapor deposited graphene are investigated via a weak localization magnetoresistance measurement. Annealing at 300 °C in inert gases, a common cleaning procedure for graphene devices, is found to raise the dephasing rate significantly above the rate from electron-electron interactions, which would otherwise be expected to dominate dephasing at 4 K and below. This extra dephasing is apparently induced by local magnetic moments activated by the annealing process, and depends strongly on the backgate voltage applied.

DOI: 10.1103/PhysRevB.105.195414

I. INTRODUCTION

The first graphene samples made into electronic devices came from flakes exfoliated from bulk graphite, and were only a few microns in size [1,2]. The discovery that graphene could also be grown over large areas, using a chemical vapor deposition (CVD) process on metal films, opened up many technological possibilities that were unimaginable with exfoliated flakes. One application proposed in the early days of graphene research was spintronics, making use of potentially long spin lifetimes in carbon-based materials. Although the hope of graphene spintronics persists, experimental realizations remain less impressive than theoretical proposals [3,4].

Despite the promise of CVD-grown graphene for technology, this growth technique tends to yield samples with more defects, such as carbon vacancies and domain boundaries, compared to exfoliated graphene [5]. In fact, defects like those found in CVD graphene are believed to be a potential source of magnetic moments that would spoil spintronic applications [6]. At the same time, the interaction of magnetic moments with conduction electrons in graphene is predicted to be different than what is observed in conventional metals, offering new avenues to realize correlated electronic states [7].

Here, we present an unexpected characteristic of defects in CVD graphene: we show that the relatively gentle annealing process typically used to remove residues from graphene devices [8–14] significantly enhances the quantum mechanical phase-breaking (dephasing) rate measured via weak localization (WL) [15], and that this dephasing is due to the activation of magnetic moments. Although data from phase coherent measurements at cryogenic temperatures might seem unrelated to applications at room temperature, our results imply that these activated defects create a fast mechanism for spin relaxation that would limit the use of CVD graphene in spintronics. At the same time, this finding sheds light on the microscopic origin of local moments in this form of graphene, and demonstrates that samples grown by CVD will be a fruitful platform to study interactions between magnetic moments and electrons in graphene.

II. EXPERIMENTAL METHODS

Multiple samples were prepared by transferring commercial CVD graphene (ACS Materials Co., MA) onto n-doped Si wafers with a 295 nm SiO_x dielectric. In some samples, a 30 nm HfO_2 film was grown by atomic layer deposition (ALD) at 100 °C on the SiO_x before transferring graphene (Supplemental Material Fig. S1, inset [16]). Hall bars with a width and a length of 30 μm × 30 μm were defined by electron beam lithography. Cr/Au (5/80 nm) Ohmic contacts were used to apply a bias current, I, and measure longitudinal and transverse voltages, V_{xx} and V_{xy} [Fig. 1(a)]; then V_{xx} was converted into resistivity ρ or conductivity $\sigma \equiv \rho^{-1}$ using the geometric aspect ratio of the Hall bar. The carrier density, n_s, was tuned using the backgate voltage, V_G, and measured via low-field Hall effect.

Samples were then annealed in Ar, N_2, forming gas (5% H_2/95% N_2; hereafter H_2/N_2), or under vacuum, using a simple thermal annealer [Fig. 1(b)]. Samples wire-bonded into ceramic chip carriers were loaded into the annealer, then pumped to a base pressure of 3×10^{-3} mbar (gas anneal) or $< 10^{-5}$ mbar (vacuum anneal). For gas annealing, the chamber was pumped and flushed; then the flow rate was adjusted using a needle valve until a pressure of 200 mbar was attained. Except where noted, samples were annealed for 1 h at 300 °C, then cooled to room temperature in the same atmosphere as the annealing step, and immediately transferred to the cryostat. After evacuating the cryostat and adding He exchange gas, samples were cooled to 4.2 K for measurement. The total air exposure time after annealing was less than 1 min.

[*]hshin@phas.ubc.ca
[†]Present address: National Research Council Canada, Edmonton, Alberta T6G 2M9, Canada.
[‡]jfolk@physics.ubc.ca

 ©2022 American Physical Society

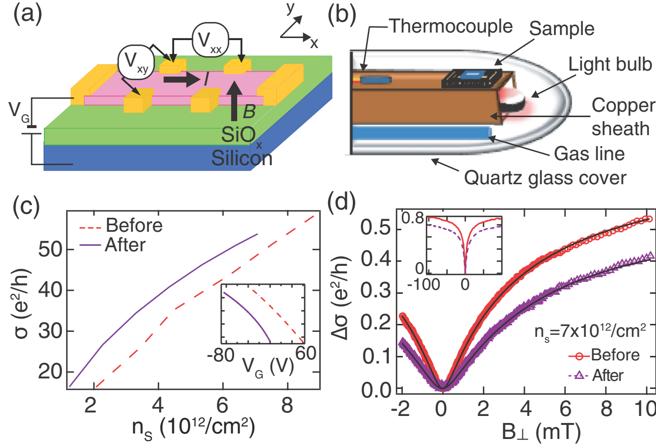

FIG. 1. (a) Schematic of the sample geometry and measurement setup. Pink indicates CVD graphene; yellow indicates Au/Cr electrodes. The dielectric stack shown here includes the SiO_x. (b) Schematic of the thermal annealing setup. (c) Change in conductivity as a function of charge carrier density, before and after Ar annealing. Inset: same data as a function of gate voltage. (d) Magnetoconductivity before and after Ar annealing, with fits to WL theory. Fit parameters before annealing: $\tau_i^{-1} = 160 \pm 45$ ns^{-1}, $\tau_\varphi^{-1} = 33 \pm 2$ ns^{-1}; after annealing: $\tau_i^{-1} = 215 \pm 90$ ns^{-1}, $\tau_\varphi^{-1} = 60 \pm 5$ ns^{-1}. Fits included data over a larger field range [16].

III. RESULTS AND DISCUSSION

Figure 1(c) compares $\sigma(n_s)$ of a sample before and after annealing in Ar. The conductivity itself rose slightly, while the gate voltage required to reach the charge neutrality point, $V_{n=0}$, decreased from 88 to 18 V. The quantum correction to the perpendicular magnetoconductivity, $\sigma(B_\perp)$, also changed after annealing [Fig. 1(d)]. To interpret this change, phase (τ_φ^{-1}) and intervalley (τ_i^{-1}) scattering rates were extracted from $\Delta\sigma(B_\perp) \equiv \sigma(B_\perp) - \sigma(0)$ using fits to the standard WL expression for graphene [15,17],

$$\Delta\sigma(B_\perp) = \frac{e^2}{\pi\hbar}\left[F\left(\frac{\tau_B^{-1}}{\tau_\varphi^{-1}}\right) - F\left(\frac{\tau_B^{-1}}{\tau_\varphi^{-1} + 2\tau_i^{-1}}\right)\right], \quad (1)$$

where $\tau_B^{-1} = 4eDB_\perp/\hbar$, $F(z) = \ln(z) + \psi(0.5 + z^{-1})$, diffusion constant $D = \frac{\sigma\pi\hbar v_f}{2e^2\sqrt{\pi n_s}}$, and $v_f = 10^6$ m/s for graphene. A third term reflecting intravalley scattering is omitted here for clarity as it did not affect the extracted τ_φ^{-1} or τ_i^{-1}, but was included in the fitting [16].

Both τ_i^{-1} and τ_φ^{-1} rose due to annealing. The rise in τ_i^{-1} reflects increased short-range scattering due to changes in the interaction between graphene and SiO_x dielectric, caused by the annealing itself [11]. The significant rise in the dephasing rate τ_φ^{-1} is more surprising, and is the central focus of this work.

Electron-electron (e-e) and electron-phonon (e-p) interactions are well known dephasing mechanisms in metallic systems. Below 50 K in graphene the e-e rate dominates, and at 4 K the e-p rate is negligible in comparison [15,18–22]. The e-e dephasing rate in graphene is [15,17,20,22,23]

$$\tau_{ee}^{-1} = \frac{k_B T}{\hbar}\left(\frac{\ln\left(\frac{g}{2}\right)}{g}\right), \qquad g = \frac{\sigma h}{e^2}. \quad (2)$$

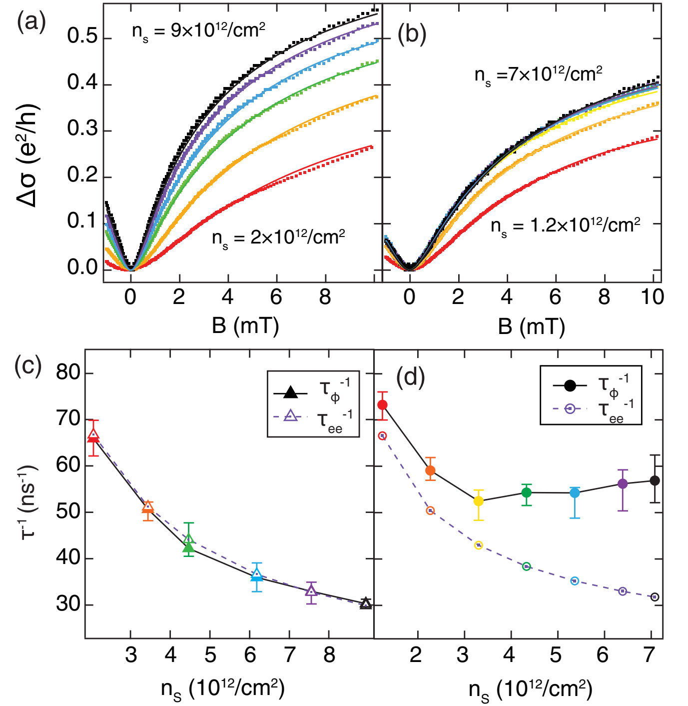

FIG. 2. The change of magnetoconductivity $\Delta\sigma(B) \equiv \sigma(B) - \sigma(B = 0)$ with carrier density before (a) and after (b) annealing in Ar. Dephasing rates τ_φ^{-1}, extracted from $\Delta\sigma(B)$ for each carrier density (filled/solid) compared with e-e rates calculated using Eq. (2) (open/dashed), before (c) and after (d) annealing. Error bars indicate range of possible values from fitting.

For the data in Fig. 1(d), Eq. (2) predicts $\tau_{ee}^{-1} = 33$ ns^{-1} before annealing, matching the measured value $\tau_\varphi^{-1} = 33 \pm 2$ ns^{-1}. After annealing, the calculated value from Eq. (2) is barely changed, $\tau_{ee}^{-1} = 32$ ns^{-1}, but the measured value rises to $\tau_\varphi^{-1} = 60 \pm 5$ ns^{-1}. Figure 2 extends this analysis to a range of n_s. Before annealing, measured τ_φ^{-1} coincide almost exactly with calculated τ_{ee}^{-1} [Fig. 2(c)]. After annealing, on the other hand, τ_φ^{-1} exceeds τ_{ee}^{-1} everywhere, with the difference, $\tau_{xs}^{-1} \equiv \tau_\varphi^{-1} - \tau_{ee}^{-1}$, growing larger with n_s [Fig. 2(d)]. Taken together, Figs. 2(c) and 2(d) indicate that e-e interaction dominates dephasing in samples as deposited, but new interactions emerge in Ar-annealed samples that add tens of ns^{-1} of excess dephasing.

As an inert gas, Ar is not expected to create chemical modifications to graphene at temperatures of only a few hundred °C. Indeed, transmission electron microscope investigations have confirmed that anneals such as those performed here do not affect perfect graphene, but that polymer resists and other residues begin to break down in the 150–250 °C temperature range, and radicals formed during that process may interact with dangling bonds at graphene defect sites [8]. Such residues are known to be ubiquitous and tenacious in samples processed using poly(methyl methacrylate) (PMMA), as was required for the electron beam lithography in our device fabrication. Our observations are consistent with the reports of Ref. [8], that the influence of annealing on defect activation is via the thermal decomposition of residues rather than the gas itself.

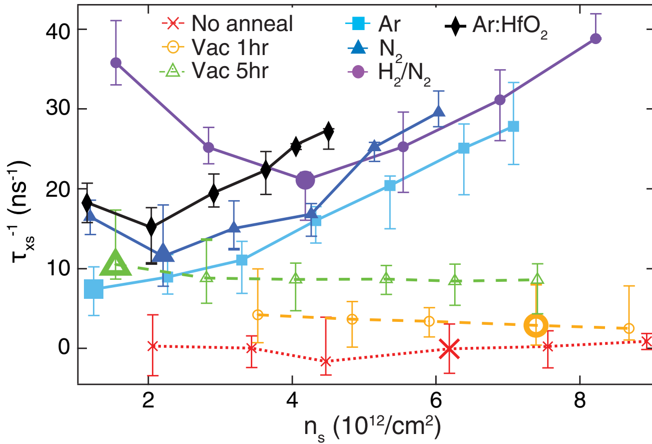

FIG. 3. The excess dephasing rate ($\tau_{xs}^{-1} \equiv \tau_{\varphi}^{-1} - \tau_{ee}^{-1}$) as a function of n_s, for various annealing conditions: no anneal; anneal in vacuum for 1 or 5 h; and anneal 1 h in Ar, N_2, or H_2/N_2. Longer anneals in gas environments were not investigated here. Samples are directly on SiO_x except where noted (Ar:HfO_2, black diamonds). Larger symbols indicate the data point corresponding to $V_G = 0$ for each recipe (for Ar:HfO_2, that point is off the graph and not shown).

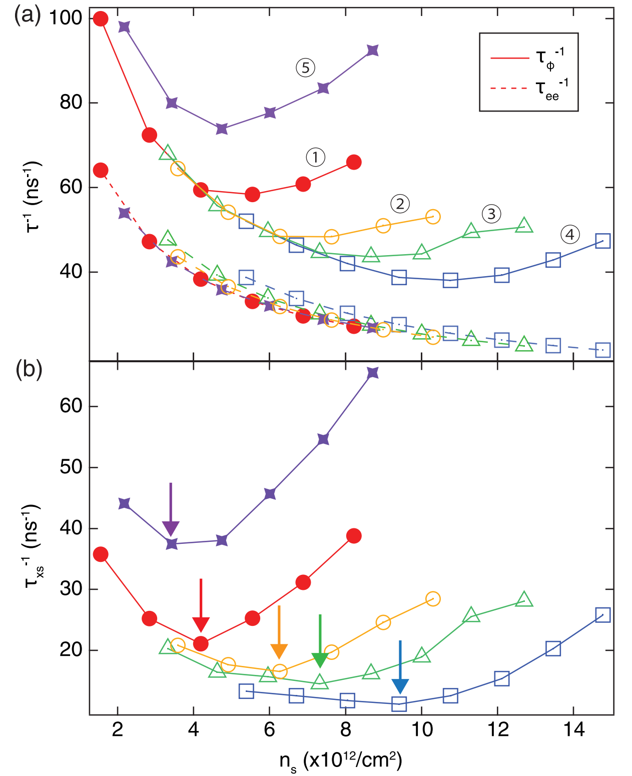

FIG. 4. (a) Evolution of the dephasing rate (solid lines) and e-e interaction rate (dashed lines), shown as a function of carrier density, for an H_2/N_2 annealed sample after air exposure. ① represents the sample immediately after 1-h H_2/N_2 anneal, ②–④ after consecutive air exposures, then ⑤ after one more H_2/N_2 anneal (b) τ_{xs}^{-1} calculated from the data in (a), with arrows indicating $V_G = 0$.

Figure 3 compiles the excess dephasing rate, τ_{xs}^{-1}, for a variety of annealing recipes, and leads to several observations. When annealing is performed in vacuum, τ_{xs}^{-1} is very small, rising only to ∼10 ns^{-1} (constant in n_s) even after 5 h of annealing. For anneals in a gas environment, on the other hand, τ_{xs}^{-1} is significantly larger, growing with n_s by an amount that does not depend on the choice of gas. τ_{xs}^{-1} also increases at low n_s, most noticeably for samples annealed in H_2/N_2. The fact that τ_{xs}^{-1} is strongly enhanced by annealing for all annealing gases tested strongly supports the hypothesis that the origin of enhanced dephasing comes from thermal decomposition of PMMA rather than from an interaction between the specific annealing gas and the graphene. The much smaller increase in τ_{xs}^{-1} when annealing in vacuum may indicate that an important role of the annealing gas is to increase the interaction time between graphene and gaseous decomposition products.

We next turn to an examination of how τ_{xs}^{-1} depends on n_s, and on the V_G that is used to tune n_s. In general, graphene's carrier density is capacitively controlled by the gate voltage but may be offset from $n_s = 0$ at $V_G = 0$ due to localized charges in the substrate, sometimes referred to as offset charges. For graphene on SiO_x, the finite gate voltage required to reach charge neutrality, $V_{n=0}$, is often dominated by offset charges coming from H_2O adsorption [24]. Annealing in various gases can desorb the H_2O, reducing this offset charge and bringing $V_{n=0}$ closer to 0. In Fig. 1, for example, $V_{n=0}$ is 88 V before annealing, dropping to 18 V after the Ar anneal.

By comparing the $\tau_{xs}^{-1}(n_s)$ line shape for different annealing conditions (leading to different $V_{n=0}$), the separate roles of offset charge, gate voltage, and total carrier density may be disentangled. Figure 3 shows that $\tau_{xs}^{-1}(n_s)$ is affected by the change in offset charge due to annealing in a surprisingly simple way: Although $V_{n=0}$ was much larger for H_2/N_2 ($V_{n=0}$ = 60 V) compared to Ar ($V_{n=0}$ = 18 V) or N_2 ($V_{n=0}$ = 31 V), the minimum in τ_{xs}^{-1} remains at the value of n_s corresponding to $V_G = 0$, that is, the larger markers in Fig. 3. This correlation seems to imply that the line shape of $\tau_{xs}^{-1}(n_s)$ depends not only on the carrier density, n_s, that includes both capacitive and offset charge contributions, but also includes a direct dependence on the absolute value of V_G.

Further insight into the importance of $|V_G|$, separate from the effect of n_s, is gained by measuring the n_s-dependent dephasing rate for a particular annealed sample, repeatedly shifting the Dirac point through exposure to ambient atmosphere (Fig. 4) [25]. ① represents τ_{φ}^{-1} for the sample immediately after an hour of annealing in H_2/N_2 ($V_{n=0}$ = 60 V), ②–④ represent subsequent 1-h exposures to ambient atmosphere ($V_{n=0}$ = 92, 109, 140 V), then ⑤ represents an additional 1-h anneal in H_2/N_2 ($V_{n=0}$=70 V). Calculated τ_{ee}^{-1} for the different exposures fall along a single curve [Fig. 4(a)], reflecting the fact that $\sigma(n_s)$ does not change through these different steps. Measured τ_{φ}^{-1} also fall along a single curve for the low-n_s part of each scan, for ①–④. However, the onset of the upturn in τ_{xs}^{-1} at high n_s shifts to higher and higher densities with exposure to air, while the minimum in τ_{xs}^{-1} remains pinned to $V_G = 0$ [arrows in Fig. 4(b)]. This behavior may indicate that the upturns in τ_{φ}^{-1} and τ_{xs}^{-1} at high density are connected to the electric field between the graphene and the backgate rather than to the carrier density itself.

The persistent upturn in τ_{xs}^{-1} at large n_s (strongly negative V_G), even after extended exposure to air, indicates that the

activation of a dephasing mechanism by annealing is robust. A second annealing step (⑤) following the multiple exposures to air results in $V_{n=0}$ shifting back to 70 V, while τ_{xs}^{-1} increases above even the values observed after the first anneal (①). As was the case for ①–④, the minimum in τ_{xs}^{-1} remains at $V_G = 0$.

Just as the activated dephasing mechanism does not seem to depend on the choice of annealing gas, it also does not depend on the substrate. In order to test for a possible influence from the substrate [26–29], Fig. 3 includes data from a sample, annealed in Ar gas, on a wafer where ALD-grown HfO_2 covers the SiO_x (Fig. S1, inset). HfO_2 layers are amorphous when grown at the low temperatures used here, presumably with a defect density and type different from those found in thermal silicon oxide [30]. The mobility of the HfO_2 sample was similar to the samples on SiO_x, in contrast to previous reports of mobility enhancement by screening due to high-κ dielectrics [31,32]; this may indicate that the mobility in our samples is limited by defects in the graphene rather than charged-impurity scattering. More importantly, the measured τ_{xs}^{-1} for the HfO_2 sample is nearly identical to that of the SiO_x sample [16]. From this, we tentatively conclude that the defects relevant to the dephasing enhancement lie in or adjacent to the graphene itself, rather than in the substrate.

The role of annealing temperature was also explored (data not shown). Below 200 °C, annealing had a minimal effect on τ_{xs}^{-1} for any of the inert gases. At 250 °C the effect was similar to, though less strong than, the 300 °C data shown here. For anneals at 350 °C and above, the excess dephasing was even larger but the graphene mobility was degraded.

IV. DEPHASING MECHANISM

The effect of an in-plane magnetic field on WL can reveal spin-related mechanisms for dephasing. Magnetic fields, $B_\parallel$, applied in the plane of a graphene sheet influence $\sigma(B_\perp)$ in two ways. First, ripples in the graphene create an out-of-plane local magnetic field, fluctuating randomly across the graphene even when $B_\parallel$ is applied exactly along the average plane of the sample. These out-of-plane components break time-reversal symmetry locally, yielding an additional dephasing mechanism that grows quadratically with $B_\parallel$ [33]. Second, $B_\parallel$ aligns local magnetic moments with Landé g-factor g once $g\mu_B B_\parallel \gg k_B T$. When free to rotate, these moments contribute to dephasing through spin-flip scattering of conduction electrons, but that mechanism is suppressed when the moments are aligned by $B_\parallel$ [33–35].

Cooling the graphene samples in a dilution refrigerator equipped with a two-axis magnet enabled $\sigma(B_\perp)$ measurements with finite $B_\parallel$, at temperatures low enough that spins could be aligned by $B_\parallel$ before dephasing due to ripples was significant. Figure 5 shows WL data for an H_2/N_2-annealed

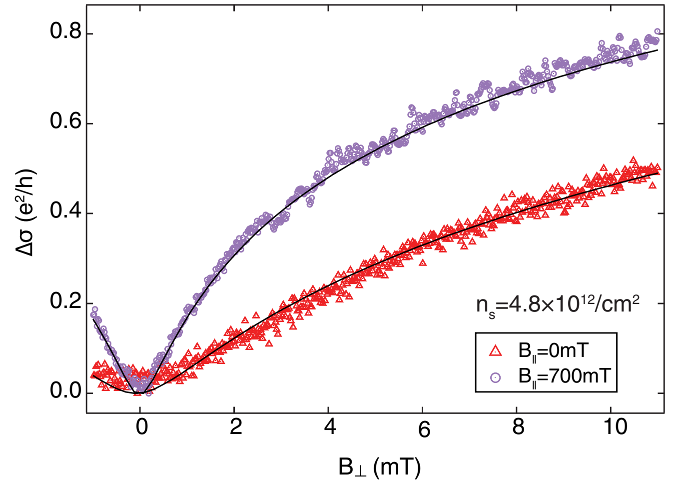

FIG. 5. Perpendicular field magnetoconductivity line shape, $\Delta\sigma(B_\perp)$, for an H_2N_2-annealed sample changes dramatically with in-plane magnetic field, $B_\parallel$. Solid lines are fits to Eq. (1). Extracted τ_φ^{-1} decreases from 95 ± 10 ns^{-1} at $B_\parallel = 0$, to 24 ± 3 ns^{-1} at $B_\parallel =$ 700 mT ($T = 100$ mK).

sample at 100 mK. (This sample was annealed at 350 °C to maximize τ_{xs}^{-1}.) The line shape of $\sigma(B_\perp)$ changes when in-plane field is applied, and fits to Eq. (1) confirm that τ_φ^{-1} drops from 95 ns^{-1} ($B_\parallel = 0$) to 24 ns^{-1} at $B_\parallel = 0.7$ T, where $g\mu_B B_\parallel / k_B T \sim 10$ with $g = 2$. Ripples would have induced the opposite effect (increased τ_φ^{-1} for higher $B_\parallel$). This data shows that spin flips induced by magnetic moments are the predominant mechanism for excess dephasing after annealing, contributing at least 70 ns^{-1}.

Magnetic moments are believed to emerge at graphene defects, including vacancies [6,36], impurities [4,37], and strain fluctuations [38,39]. In most cases, the interactions of defect-bound moments with conduction electrons are predicted to strengthen at low carrier density due to weaker screening [6,36,40,41]. We find, in contrast, that τ_{xs}^{-1} increases at higher n_s and, more importantly, depends more on the electric field due to V_G than on the carrier density itself since gas-annealed samples show the minimum near $V_G = 0$. It may be, therefore, that the magnetic moments being activated by gas annealing are of a different type than has been previously reported in experiment or studied theoretically.

ACKNOWLEDGEMENTS

Experiments were undertaken with support from the Stewart Blusson Quantum Matter Institute, the Natural Sciences and Engineering Research Council of Canada, the Canada Foundation for Innovation, the Canadian Institute for Advanced Research, and the Canada First Research Excellence Fund, Quantum Materials and Future Technologies Program.

[1] A. H. Castro Neto, F. Guinea, N. M. R. Peres, K. S. Novoselov, and A. K. Geim, The electronic properties of graphene, Rev. Mod. Phys. **81**, 109 (2009).

[2] A. K. Geim and K. S. Novoselov, The rise of graphene, *Nanoscience and Technology: A Collection of Reviews from Nature Journals* (World Scientific, Singapore, 2010), p. 11.

[3] A. Avsar, H. Ochoa, F. Guinea, B. Özyilmaz, B. J. van Wees, and I. J. Vera-Marun, *Colloquium*: Spintronics in graphene and other two-dimensional materials, Rev. Mod. Phys. **92**, 021003 (2020).

[4] W. Han and R. K. Kawakami, Spin Relaxation in Single-Layer and Bilayer Graphene, Phys. Rev. Lett. **107**, 047207 (2011).

[5] H. C. Lee, W.-W. Liu, S.-P. Chai, A.-R. Mohamed, A. Aziz, C.-S. Khe, N. M. S. Hidayah, and U. Hashim, Review of the synthesis, transfer, characterization and growth mechanisms of single and multilayer graphene, RSC Adv. **7**, 15644 (2017).

[6] O. V. Yazyev and L. Helm, Defect-induced magnetism in graphene, Phys. Rev. B **75**, 125408 (2007).

[7] Z. Shi, E. M. Nica, and I. Affleck, Kondo effect due to a hydrogen impurity in graphene: A multichannel Kondo problem with diverging hybridization, Phys. Rev. B **100**, 125158 (2019).

[8] Y.-C. Lin, C.-C. Lu, C.-H. Yeh, C. Jin, K. Suenaga, and P.-W. Chiu, Graphene annealing: How clean can it be? Nano Lett. **12**, 414 (2012).

[9] M. Ishigami, J. H. Chen, W. G. Cullen, M. S. Fuhrer, and E. D. Williams, Atomic structure of graphene on SiO_2, Nano Lett. **7**, 1643 (2007).

[10] Y. Dan, Y. Lu, N. J. Kybert, Z. Luo, and A. T. Johnson, Intrinsic response of graphene vapor sensors, Nano Lett. **9**, 1472 (2009).

[11] Z. Cheng, Q. Zhou, C. Wang, Q. Li, C. Wang, and Y. Fang, Toward intrinsic graphene surfaces: A systematic study on thermal annealing and wet-chemical treatment of SiO_2-supported graphene devices, Nano Lett. **11**, 767 (2011).

[12] A. Pirkle, J. Chan, A. Venugopal, D. Hinojos, C. W. Magnuson, S. McDonnell, L. Colombo, E. M. Vogel, R. S. Ruoff, and R. M. Wallace, The effect of chemical residues on the physical and electrical properties of chemical vapor deposited graphene transferred to SiO_2, Appl. Phys. Lett. **99**, 122108 (2011).

[13] C. R. Dean, A. F. Young, I. Meric, C. Lee, L. Wang, S. Sorgenfrei, K. Watanabe, T. Taniguchi, P. Kim, K. L. Shepard *et al.*, Boron nitride substrates for high-quality graphene electronics, Nat. Nanotechnol. **5**, 722 (2010).

[14] W. S. Leong, C. T. Nai, and J. T. L. Thong, What does annealing do to metal–graphene contacts? Nano Lett. **14**, 3840 (2014).

[15] F. V. Tikhonenko, D. W. Horsell, R. V. Gorbachev, and A. K. Savchenko, Weak Localization in Graphene Flakes, Phys. Rev. Lett. **100**, 056802 (2008).

[16] See Supplemental Material at http://link.aps.org/supplemental/10.1103/PhysRevB.105.195414 for further details on the experiment.

[17] E. McCann, K. Kechedzhi, V. I. Fal'ko, H. Suzuura, T. Ando, and B. L. Altshuler, Weak-Localization Magnetoresistance and Valley Symmetry in Graphene, Phys. Rev. Lett. **97**, 146805 (2006).

[18] B. L. Altshuler, D. Khmel'nitzkii, A. I. Larkin, and P. A. Lee, Magnetoresistance and Hall effect in a disordered two-dimensional electron gas, Phys. Rev. B **22**, 5142 (1980).

[19] A. A. Kozikov, A. K. Savchenko, B. N. Narozhny, and A. V. Shytov, Electron-electron interactions in the conductivity of graphene, Phys. Rev. B **82**, 075424 (2010).

[20] I. L. Aleiner, B. L. Altshuler, and M. E. Gershenson, Interaction effects and phase relaxation in disordered systems, Waves Random Media **9**, 201 (1999).

[21] F. V. Tikhonenko, A. A. Kozikov, A. K. Savchenko, and R. V. Gorbachev, Transition between Electron Localization and Antilocalization in Graphene, Phys. Rev. Lett. **103**, 226801 (2009).

[22] K.-J. Min, J. Park, W.-S. Kim, and D.-H. Chae, Asymmetric electron-hole decoherence in ion-gated epitaxial graphene, Sci. Rep. **7**, 1 (2017).

[23] B. L. Altshuler, A. G. Aronov, and D. E. Khmelnitsky, Effects of electron-electron collisions with small energy transfers on quantum localisation, J. Phys. C **15**, 7367 (1982).

[24] P. Joshi, H. E. Romero, A. T. Neal, V. K. Toutam, and S. A. Tadigadapa, Intrinsic doping and gate hysteresis in graphene field effect devices fabricated on SiO_2 substrates, J. Phys.: Condens. Matter **22**, 334214 (2010).

[25] H. Liu, Y. Liu, and D. Zhu, Chemical doping of graphene, J. Mater. Chem. **21**, 3335 (2011).

[26] J. J. Van Den Berg, R. Yakimova, and B. J. Van Wees, Spin transport in epitaxial graphene on the C-terminated $(000\bar{1})$-face of silicon carbide, Appl. Phys. Lett. **109**, 012402 (2016).

[27] K. Chen, X. Wang, J.-B. Xu, L. Pan, X. Wang, and Y. Shi, Electronic properties of graphene altered by substrate surface chemistry and externally applied electric field, J. Phys. Chem. C **116**, 6259 (2012).

[28] S. Scarfe, W. Cui, A. Luican-Mayer, and J. M. Ménard, Systematic THz study of the substrate effect in limiting the mobility of graphene, Sci. Rep. **11**, 8729 (2021).

[29] M. Poljak, T. Suligoj, and K. L. Wang, Influence of substrate type and quality on carrier mobility in graphene nanoribbons, J. Appl. Phys. **114**, 053701 (2013).

[30] D. M. Hausmann and R. G. Gordon, Surface morphology and crystallinity control in the atomic layer deposition (ALD) of hafnium and zirconium oxide thin films, J. Cryst. Growth **249**, 251 (2003).

[31] F. Chen, J. Xia, D. K. Ferry, and N. Tao, Dielectric screening enhanced performance in graphene FET, Nano Lett. **9**, 2571 (2009).

[32] A. Konar, T. Fang, and D. Jena, Effect of high-κ gate dielectrics on charge transport in graphene-based field effect transistors, Phys. Rev. B **82**, 115452 (2010).

[33] M. B. Lundeberg and J. A. Folk, Rippled Graphene in an In-Plane Magnetic Field: Effects of a Random Vector Potential, Phys. Rev. Lett. **105**, 146804 (2010).

[34] M. B. Lundeberg, R. Yang, J. Renard, and J. A. Folk, Defect-Mediated Spin Relaxation and Dephasing in Graphene, Phys. Rev. Lett. **110**, 156601 (2013).

[35] D. Kochan, M. Gmitra, and J. Fabian, Spin Relaxation Mechanism in Graphene: Resonant Scattering by Magnetic Impurities, Phys. Rev. Lett. **112**, 116602 (2014).

[36] J.-J. Chen, H.-C. Wu, D.-P. Yu, and Z.-M. Liao, Magnetic moments in graphene with vacancies, Nanoscale **6**, 8814 (2014).

[37] C. Józsa, T. Maassen, M. Popinciuc, P. J. Zomer, A. Veligura, H. T. Jonkman, and B. J. van Wees, Linear scaling between momentum and spin scattering in graphene, Phys. Rev. B **80**, 241403(R) (2009).

[38] N. J. G. Couto, D. Costanzo, S. Engels, D.-K. Ki, K. Watanabe, T. Taniguchi, C. Stampfer, F. Guinea, and A. F. Morpurgo, Random Strain Fluctuations as Dominant Disorder Source for High-Quality On-Substrate Graphene Devices, Phys. Rev. X **4**, 041019 (2014).

[39] C. Neumann, S. Reichardt, P. Venezuela, M. Drögeler, L. Banszerus, M. Schmitz, K. Watanabe, T. Taniguchi, F. Mauri, B. Beschoten *et al.*, Raman spectroscopy as probe of nanometre-

scale strain variations in graphene, Nat. Commun. **6**, 8429 (2015).

[40] P. Haase, S. Fuchs, T. Pruschke, H. Ochoa, and F. Guinea, Magnetic moments and Kondo effect near vacancies and resonant scatterers in graphene, Phys. Rev. B **83**, 241408(R) (2011).

[41] S. Engels, B. Terrés, A. Epping, T. Khodkov, K. Watanabe, T. Taniguchi, B. Beschoten, and C. Stampfer, Limitations to Carrier Mobility and Phase-Coherent Transport in Bilayer Graphene, Phys. Rev. Lett. **113**, 126801 (2014).